

## Absence of superconductivity in micrometer-sized $\varepsilon$ -NbN single crystals

Fan-Yun Chiu,<sup>1,2,3,\*</sup> Tsu-Lien Hung<sup>2,\*</sup>,† Cheng-Yen Liu<sup>2</sup>, Ya-Hsin Pai<sup>2</sup>, Wei-Liang Chien,<sup>4</sup> Peng-Jen Chen,<sup>5,6</sup> Ting-Kuo Lee,<sup>2,7</sup> Ming-Jye Wang<sup>2,8</sup>, Min-Nan Ou<sup>2,‡</sup>, Chang C. Tsuei,<sup>2</sup> Maw-Kuen Wu,<sup>2</sup> Chia-Seng Chang,<sup>1,2,3</sup> and Yang-Yuan Chen<sup>2,9,§</sup>

<sup>1</sup>Department of Physics, National Taiwan University, Taipei 106319, Taiwan, Republic of China

<sup>2</sup>Institute of Physics, Academia Sinica, Taipei 115201, Taiwan, Republic of China

<sup>3</sup>Nano science and Technology program, Taiwan International Graduate Program, Taipei 115201, Taiwan, Republic of China

<sup>4</sup>Department of Materials Science and Engineering, National Taiwan University, Taipei 106319, Taiwan, Republic of China

<sup>5</sup>Department of Mechanical Engineering, City University of Hong Kong, Kowloon, Hong Kong SAR, China

<sup>6</sup>Hong Kong Institute for Advanced Study, City University of Hong Kong, Kowloon, Hong Kong SAR, China

<sup>7</sup>Department of Physics, National Sun Yat-sen University, Kaohsiung 804201, Taiwan, Republic of China

<sup>8</sup>Institute of Astronomy and Astrophysics, Academia Sinica, Taipei 106319, Taiwan, Republic of China

<sup>9</sup>Graduate Institute of Applied Physics, National Chengchi University, Taipei 116011, Taiwan, Republic of China



(Received 1 August 2021; revised 15 April 2022; accepted 27 April 2022; published 18 May 2022)

It is important to study the properties of high quality single crystal in order to resolve the issue of an interesting material in which certain debatable fundamental properties exist. However, it is unfortunate that a sizable single crystal for experimental measurements is not always available. NbN is one of the examples; it has attracted scientific and engineering interest due to its diverse physical properties and a variety of structural phases. Until now superconductivity is only observed in cubic  $\delta$ - and tetragonal  $\gamma$ -NbN but not in hexagonal  $\varepsilon$ -NbN. Recently, Zou *et al.* reported the observation of superconductivity with  $T_c \sim 11.6$  K in a hexagonal  $\varepsilon$ -NbN based on the measurement on a multiphase powder specimen. In order to resolve the issue, the work used the electron backscattering diffraction technique to characterize phases of micron-size NbN crystals from commercial powders and measure their transport properties. Our results unambiguously confirm that the hexagonal  $\varepsilon$ -NbN phase is not superconducting.

DOI: [10.1103/PhysRevB.105.174512](https://doi.org/10.1103/PhysRevB.105.174512)

### I. INTRODUCTION

Niobium nitride has attracted a lot of attention owing to its renowned novel properties, such as high hardness, large bulk modulus, ultraincompressibility, and high shear rigidity [1]. Furthermore, the cubic  $\delta$ -NbN exhibits superconductivity with  $T_c$  up to 17 K, which has been widely applied to numerous applications, such as Josephson junctions [2], superconducting cavity [3], and superconducting hot-electron photon detectors [4]. NbN has five polymorphs, including cubic  $\delta$ - [5,6], tetragonal  $\gamma$ - [7–9], hexagonal WC- [10], hexagonal  $\delta'$ -, and hexagonal  $\varepsilon$ -NbN [11,12], as tabulated in Table I. The structure of tetragonal  $\gamma$ -NbN is distorted from cubic  $\delta$ -NbN due to the existence of nitrogen vacancy [8,9]. The three hexagonal phases of WC-,  $\varepsilon$ -, and  $\delta'$ -NbN are differentiated by the distinct position of niobium atoms. Particularly, the hexagonal  $\varepsilon$ - and  $\delta'$ -NbN have the same space group as the  $c$  axis of  $\varepsilon$ -NbN being twice that of  $\delta'$ -NbN. It has been well established that cubic  $\delta$ - and tetragonal  $\gamma$ -NbN exhibit superconductivity [13–15]. No superconductivity was reported in hexagonal phases until recently; Zou *et al.* [16] claimed it

to be superconducting with possibly topological. The report was based on the observation of superconductivity in  $\varepsilon$ -NbN powder using magnetization and resistivity measurements on a specimen containing 2% cubic  $\delta$ -NbN impurity. This report has attracted great attention due to the potential discovery of topological superconductivity in the NbN system.

Many theoretical efforts have been carried out to investigate the mechanical properties, electronic band structure, and lattice dynamics [17–19] of  $\varepsilon$ -NbN. The hexagonal phase was recognized as more stable than the cubic phase in line with the total energy calculations [19]. Recently, Chen *et al.* [20] found that  $\varepsilon$ -NbN has high-order Dirac and Weyl points. Babu *et al.* [21] reported that all four NbN bulks show the characteristic of topological insulators based on the density functional theory calculation with the generalized gradient approximation. Interestingly, they claimed that the electron-phonon coupling ( $\lambda$ ) in cubic  $\delta$ -NbN ( $\lambda = 0.98$ ) is much stronger than in hexagonal  $\varepsilon$ - ( $\lambda = 0.16$ ), WC- ( $\lambda = 0.11$ ), and  $\delta'$ -NbN ( $\lambda = 0.17$ ). This results in a much higher superconducting transition temperature ( $T_c = 18.2$  K) in cubic  $\delta$ -NbN. Besides the bulk, NbN thin films have also been extensively studied. The cubic  $\delta$ -NbN has a wide range of superconducting temperature (10.2–16.6 K) [22,23], which sensitively depends on lattice parameters and the atomic ratio of N/Nb [24–27]. Since the ratio of N/Nb and lattice parameters of films can be controlled by rf sputtering conditions via adjusting nitrogen pressure and substrate temperature [26,27], subsequently the

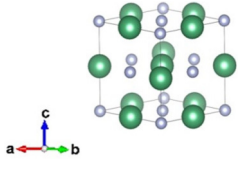
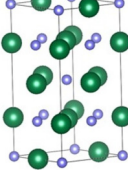
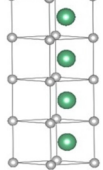
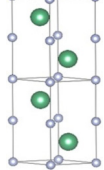
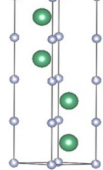
\*These authors contributed equally to this work.

†Corresponding author: poollotus0426@gmail.com

‡oumn@gate.sinica.edu.tw

§cheny2@phys.sinica.edu.tw

TABLE I. The atomic structures, space group, and  $T_c$  of NbN for cubic  $\delta$ -NbN, tetragonal  $\gamma$ -NbN, hexagonal WC-NbN, hexagonal  $\delta'$ -NbN, and hexagonal  $\varepsilon$ -NbN phases. Nitrogen and niobium are represented by gray and green symbols respectively.

	$\delta$ -NbN	$\gamma$ -NbN	WC-NbN	$\delta'$ -NbN	$\varepsilon$ -NbN
Crystal structure					
Space group	Fm-3m	I-4m2	P-6m2	P63/mmc	P63/mmc
$T_c$ of bulk	13–17.2 K [13–15]	7.8–15 K [13,14]			11.6 K <sup>a</sup> [16]
$T_c$ of film	10.2–16.6 K [20,21]				
$T_c$ in this work	11.2 K	7.6 K			

<sup>a</sup>The result is not confirmed.

physical properties of cubic  $\delta$ -NbN films can be tuned by the deposition conditions. Chen *et al.* [28] reported that the two phonon bands in cubic  $\delta$ -NbN were shifted to high frequency by increasing pressure, and raised  $T_c$  to a saturated value of 12.6 K at 42 GPa. The enhancement of  $T_c$  is attributed to the

pressure induced electronic stiffness which is in connection with the phonon frequency shifting [29]. The hexagonal  $\varepsilon$ -NbN film was grown in 1974 by annealing cubic  $\delta$ -NbN<sub>x</sub> films in H<sub>2</sub> at 1000 °C [11]. The resistivity measurements showed no superconductivity for  $T > 1.77$  K, which is consistent with the theoretical calculation [23]. Anand *et al.* computed the density of states of the monolayer hexagonal honeycomb and rectangular structures of NbN [30] and pointed out that the rectangular NbN monolayer is a superconductor, nonetheless the hexagonal honeycomb NbN monolayer is a semiconductor.

Based on the above discussion, the superconductivity in  $\varepsilon$ -NbN remains to be elucidated. The specimen studied by Zou *et al.* was powder with 2% cubic  $\delta$ -NbN impurity. Therefore, it is significant to examine superconductivity in a well characterized hexagonal  $\varepsilon$ -NbN crystal. Unfortunately, it is difficult to obtain large-size hexagonal  $\varepsilon$ -NbN single crystal, which can only be prepared using high-pressure synthesis, and typically in  $\mu\text{m}$  size. In this paper, we report

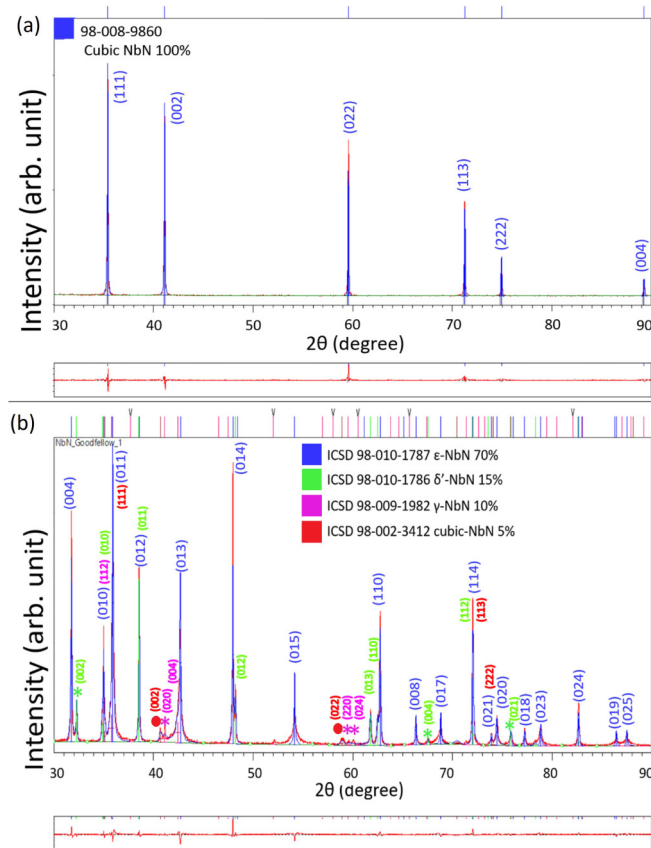


FIG. 1. Powder x-ray diffraction patterns and Rietveld refinement. (a) A pure cubic  $\delta$ -NbN powder (from Alfa Aesar, after postannealing) (ICSD no. 98-008-9860). (b) A main phase of  $\varepsilon$ -NbN powder with wt% of various phases (from Goodfellow); impurity phases are represented by symbols \* and •.

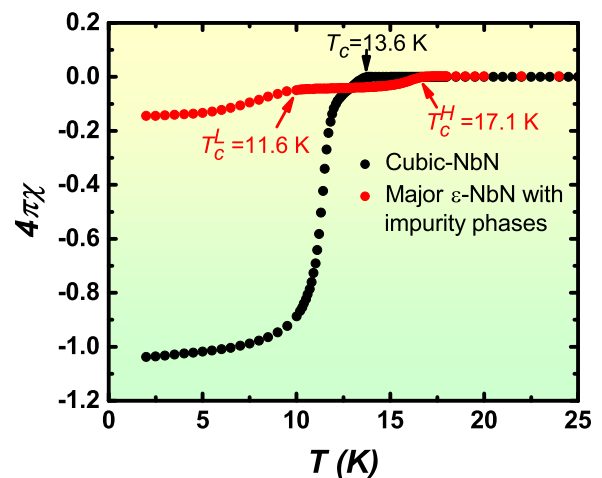


FIG. 2. The zero-field cooling (ZFC) magnetic susceptibility for the cubic  $\delta$ -NbN and the major hexagonal  $\varepsilon$ -NbN powder at a constant field 10 Oe.

TABLE II. The lattice parameters and wt % fraction for the pure cubic  $\delta$ -NbN and the major phase hexagonal  $\varepsilon$ -NbN powder. The results are calculated from the Rietveld refinement using PANalytical X'pert Highscore Plus software.

Sample	Phase component	Wt %	$a, b$ (Å)	$c$ (Å)
$\delta$ -NbN powder	$\delta$ -NbN	100%	4.385(4)	
Major phase $\varepsilon$ - NbN powder	$\varepsilon$ -NbN	70%	2.960(6)	11.269(2)
	$\delta'$ -NbN	15%	2.971(8)	5.544(9)
	$\gamma$ -NbN	10%	4.386(9)	8.619(4)
	$\delta$ -NbN	5%	4.431(5)	

the results of using an innovative approach, which combines the electron backscattering diffraction (EBSD) and a platform with patterned electrodes, to measure the resistivity of a  $\mu\text{m}$ -size hexagonal  $\varepsilon$ -NbN single crystal. Our results unambiguously show that the hexagonal  $\varepsilon$ -NbN is nonsuperconducting.

## II. EXPERIMENT

We first study the available NbN powder specimens by x-ray characterization and magnetic and specific heat measurements. The cubic  $\delta$ -NbN was prepared by annealing the on-shelf product from Alfa Aesar (batch no. J03Z045) at  $1400^\circ\text{C}$  for 3 h. The hexagonal  $\varepsilon$ -NbN powder was purchased from Goodfellow (batch no. 476442, purity 99%). The  $\varepsilon$ -NbN powder was further synthesized under conditions of 10 GPa and  $1200^\circ\text{C}$  for 1.5 h in a high-pressure multianvil apparatus. All samples were characterized by x-ray diffraction using a

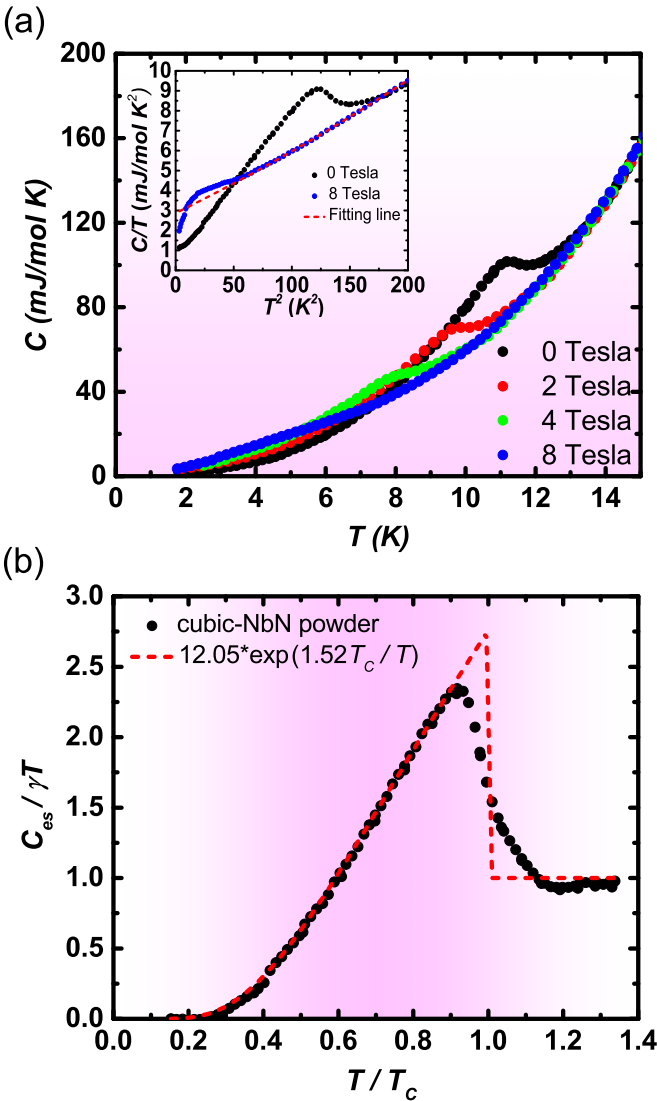


FIG. 3. (a) Temperature dependence of specific heat for cubic  $\delta$ -NbN at different magnetic fields. Inset:  $C/T$  versus  $T^2$  fit. (b) Temperature dependence of electronic specific heat in superconducting state,  $C_{es}$ . The red dashed line is fitting of BCS theory.

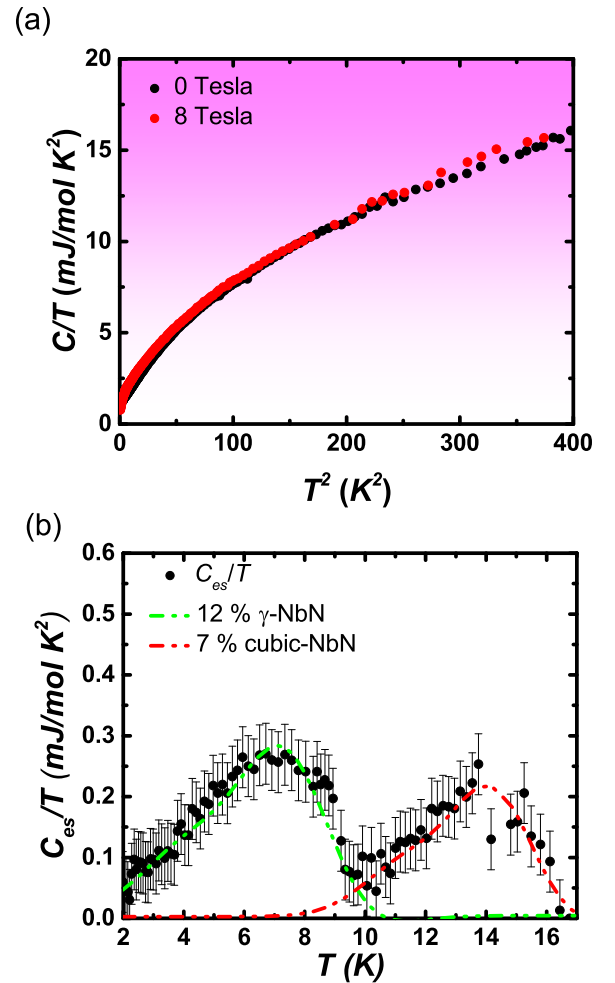


FIG. 4. (a) Temperature dependence of specific data of the major phase  $\varepsilon$ -NbN powder at 0 and 8 T, plotted as  $C/T$  versus  $T^2$ . (b) The specific heat of superconducting state is fitted to the 12% tetragonal  $\gamma$ -NbN with  $T_c$  of 6.8 K and 7% cubic  $\delta$ -NbN with  $T_c$  of 13.7 K.

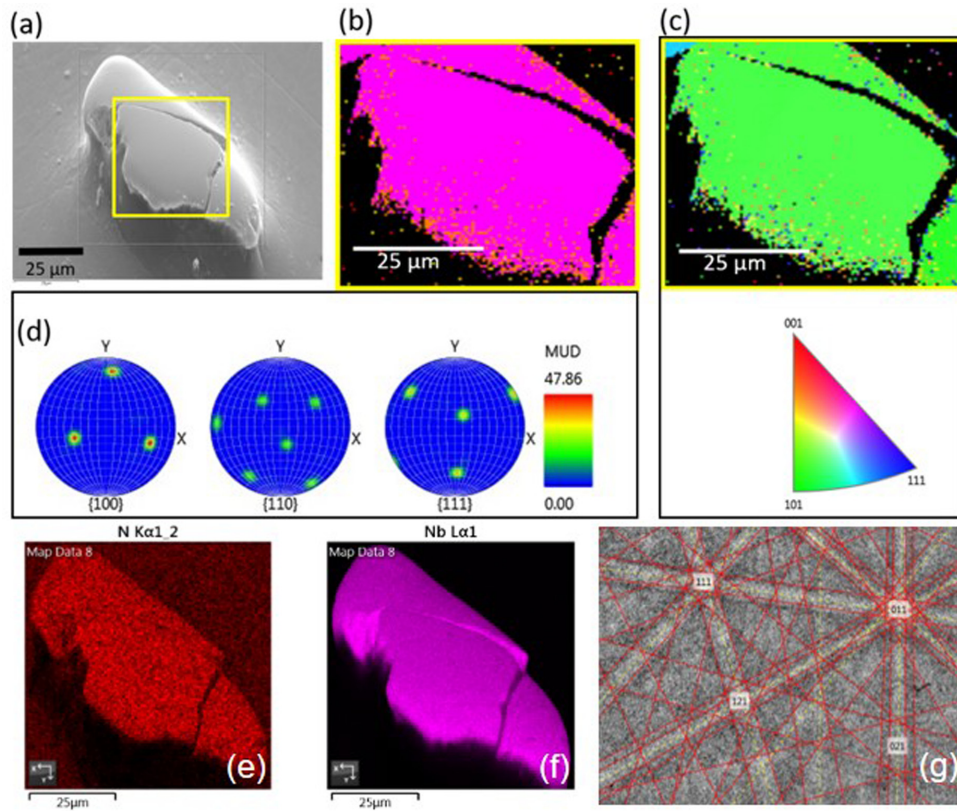


FIG. 5. (a) The SEM image of the whole specimen for the cubic  $\delta$ -NbN crystal. The part enclosed by the yellow frame was taken for RT measurements. (b) EBSD phase mapping of the whole specimen. Pink color represents the  $\delta$ -NbN phase; although the orange color is assigned to represent tetragonal  $\gamma$ -NbN, it is believed to be misjudged by the roughness near sample edge since EBSD result is very sensitive to the surface flatness. The yellow color represents  $\delta'$ -NbN and the red color represents  $\varepsilon$ -NbN; both of them are less than 2% which is in the range of measurement resolution. Panels (c) and (d) represent the measurement of crystal orientation by exam of pole figures, while (c) presents inverse pole figure mapping of the scanning plane close to the lattice plane (101) and (d) the reproduced pole figures for lattice plane {100}, {110}, and {111}. (e), (f) The *in situ* SEM EDX mapping for N- $K_{\alpha}$  and Nb- $L_{\alpha}$  lines of the crystal. (g) The overlapping of Kikuchi pattern and EBSD pattern of the crystal.

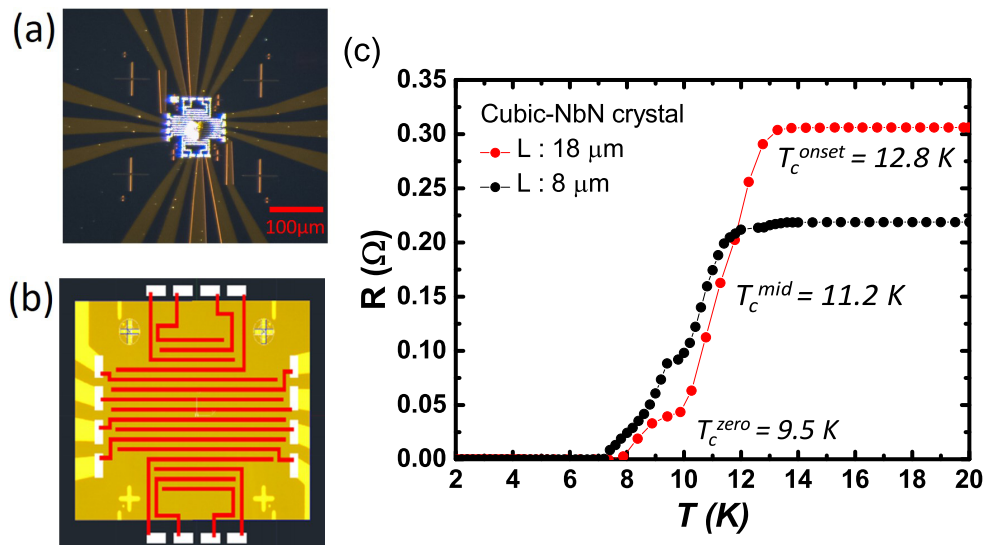


FIG. 6. (a) The image of the cubic  $\delta$ -NbN crystal loaded on an electrical measurement platform. (b) A drawing of parallel electrodes at the center of the platform. (c) Temperature dependence of electrical resistance for the cubic  $\delta$ -NbN crystal with  $50 \times 30 \mu\text{m}$  in size. The black and red curves represent different measurements using different pairs of electrodes for voltage measurement; one has  $8 \mu\text{m}$  and the other has  $18 \mu\text{m}$  in separation. A minor phase of cubic NbN with even higher nitrogen deficiency was revealed in a second drop at  $T \sim 10 \text{ K}$  for measurements with two different set of electrodes. Due to the interference of first drop the real  $T_c$  of the second drop is estimated to be  $> 10 \text{ K}$ .

powder diffractometer (PANalytical X'Pert Pro) with Cu- $K\alpha$  ( $\lambda_{K\alpha} = 1.5406 \text{ \AA}$ ) source. The magnetic susceptibility and specific heat were measured by a superconducting quantum interference device magnetometer (Quantum Design Inc.) and a homemade thermal relaxation calorimeter [30], respectively.

### III. RESULT AND DISCUSSION

The powder x-ray diffraction patterns of a cubic  $\delta$ -NbN powder and an  $\varepsilon$ -NbN powder specimen with minor impurities are displayed in Figs. 1(a) and 1(b), respectively. The results were calculated from the Rietveld refinement using PANalytical X'pert HighScore Plus with corresponding error  $\sim \pm 2\%$ . The diffraction pattern of  $\delta$ -NbN powder specimen is well fit to the characteristic peaks of the cubic structure of  $Fm-3m$  with a lattice parameter  $a = 4.385(4) \text{ \AA}$  without any impurity (Table II). On the other hand, the  $\varepsilon$ -NbN powder specimen, based on the Rietveld refinement results (Fig. 1), consists of a major phase of  $\varepsilon$ -NbN ( $\sim 70\%$ ) together with  $\delta'$ - (15%),  $\gamma$ - (10%), and  $\delta$ - (5%) NbN impurity phases. The refined lattice parameters and the weight percent for all phases are tabulated in Table II. The lattice parameters for the major phase of  $\varepsilon$ -NbN are  $a = 2.960(6) \text{ \AA}$ ,  $c = 11.269(2) \text{ \AA}$ . The lattice parameters are similar to the previous report by Zou *et al.* [16]. We note that most diffraction peaks of the  $\gamma$ -NbN phase overlap with those of the  $\varepsilon$ -NbN phase.

The magnetic susceptibilities of the cubic  $\delta$ - and the major phase hexagonal  $\varepsilon$ -NbN powder specimens are shown in Fig. 2. The susceptibility of the pure  $\delta$ -NbN powder shows a clear superconducting transition at 13.6 K with almost 100% superconducting volume fraction of the theoretical value. The data for the major phase  $\varepsilon$ -NbN powder specimen are similar to that observed by Zou *et al.* [16], i.e., two weak superconducting transitions with corresponding superconducting volume fractions  $\sim 10\%$  and  $\sim 5\%$  appear at 11.6 and 17.1 K, respectively. Comparing the  $T_c$  values of various phases [7,13,14] and the superconducting volume fractions obtained from x-ray diffraction (Table II), we come to a conclusion that the two superconducting transitions are from the minor  $\gamma$  and  $\delta$  phases respectively, and has nothing to do with the  $\varepsilon$ -NbN phase.

In order to further understand the superconductivity observed, the low temperature specific heat measurements were carried out using the thermal relaxation method [31]. The temperature dependence of specific heat of  $\delta$ -NbN at various magnetic fields is shown in Fig. 3(a) for a 20-mg compressed powder specimen. A superconductivity transition at 11.2 K with a transition width of 2.6 K was observed in specific heat at zero magnetic field. The relatively broad transition can be attributed to the integration of  $T_c$  distribution arising from the composition variation in the specimen. The  $T_c$  of  $\delta$ -NbN is clearly suppressed by the magnetic field. The low temperature specific heat of the normal state can be described by the formula  $C/T = \gamma T + \beta T^2$  [inset of Fig. 3(a)]. The derived relevant parameters are the linear coefficient of specific heat  $\gamma = 2.9 \text{ mJ/K}^2$  and  $\beta = 2.8 \times 10^{-2} \text{ mJ/K}^4 \text{ mol}$ , from which the Debye temperature  $\Theta_D$  is estimated to be 408 K using the equation  $\beta = (12/5)N\pi^4 R/\Theta_D^3$ , where  $R$  is the gas constant. Figure 3(b) depicts the plot of  $C_{es}/\gamma T$  versus  $T/T_c$  near the transition. The derived superconducting

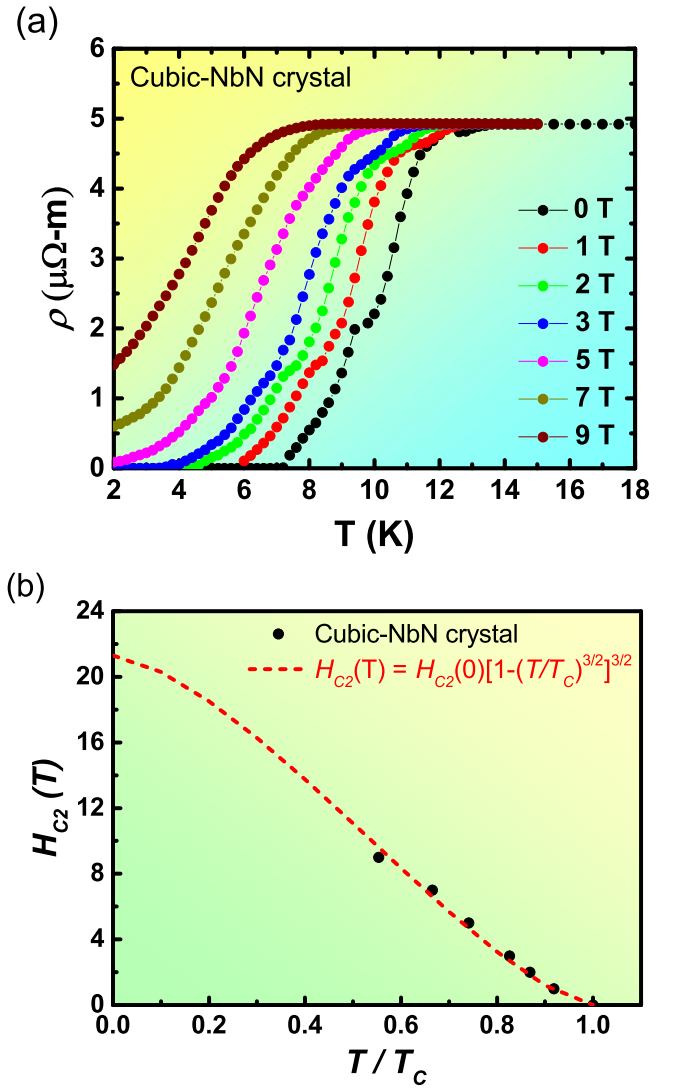


FIG. 7. (a) Temperature dependence of electrical resistivity of the cubic  $\delta$ -NbN crystal under magnetic fields 0, 1, 2, 3, 5, 7, and 9 T. (b) Upper critical field as a function of temperature. The  $T_c$  is determined from the resistivity at 90% drop from the normal state value.

heat capacity jump  $\Delta C/\gamma T_c$  is 1.7, slightly larger than the 1.43 of the Bardeen-Cooper-Schrieffer (BCS) model. Below  $T_c = 11.2 \text{ K}$ , the electronic specific heat of superconducting is obtained by fitting to an exponential formula  $C_{es}(T)/\gamma T_c = 12.05 e^{-1.52T_c/T}$ , where  $C_{es}(T) = C_{\text{total}} - C_n$ . The average superconducting energy gap  $E_g$  is about  $3.04 k_B T_c$ , which is close to the BCS value of 3.5 for an  $s$ -wave superconductor.

For the  $\varepsilon$ -NbN powder specimen, no clear specific heat anomaly associated with the superconducting transition was observed, as shown in Fig. 4(a). However, the data reveal a small but wide bump spanned in the temperature range 10–17 K. After phonon background subtraction, the data can be fit to a sum of two superconducting transitions arising from the minor phases of  $\gamma$ -NbN ( $\sim 12\%$ ) of 6.8 K and  $\delta$ -NbN (7%) of 13.7 K. The specific heat results further confirm that the superconducting transitions observed come from the minor phases of  $\gamma$ - and  $\delta$ -NbN, not from the main  $\varepsilon$ -NbN (70%) phase.

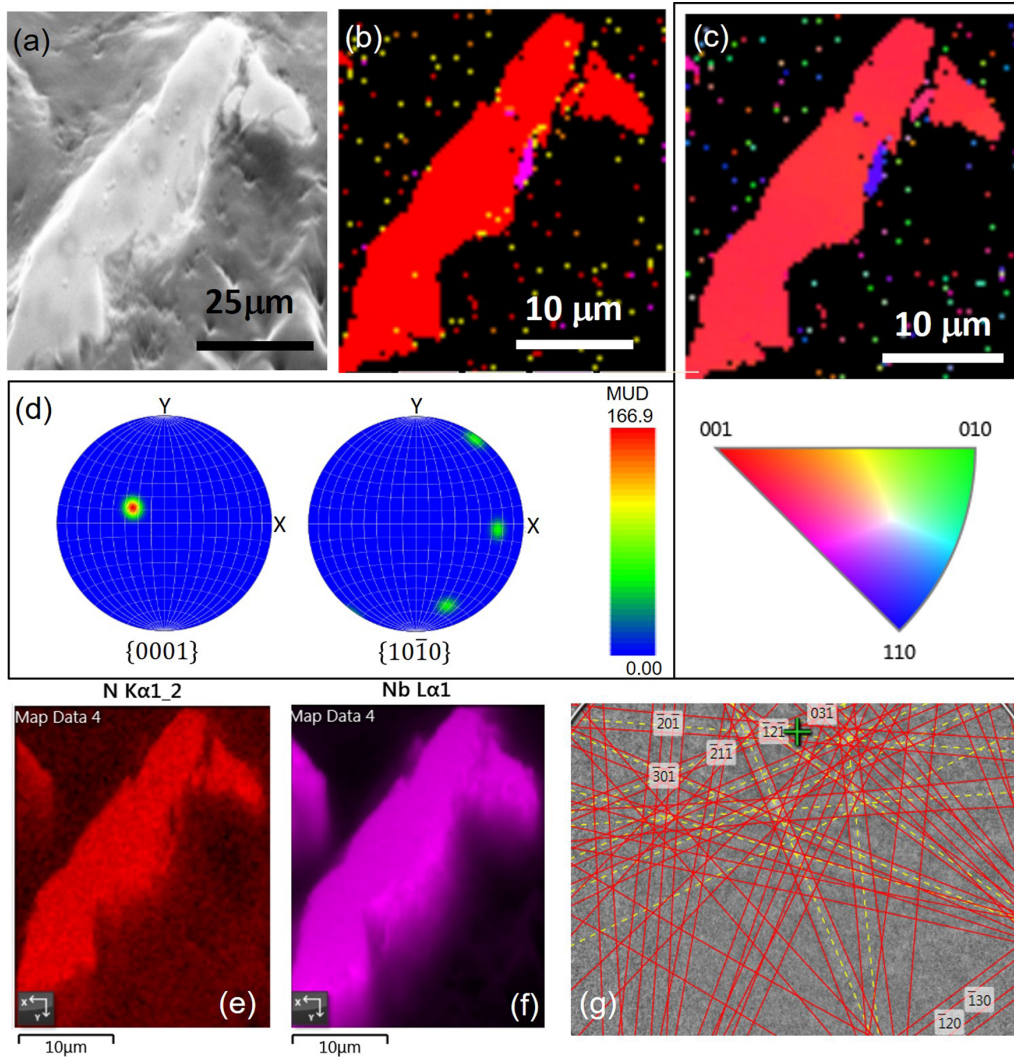


FIG. 8. (a) The SEM image of the hexagonal  $\epsilon$ -NbN crystal. (b) EBSD phase mapping of the specimen. Red color area represents  $\epsilon$ -NbN phase; a tiny pink area is believed the unevenness near sample edge. (c) Inverse pole figure mapping of the lattice plane (001). Inverse pole figure mapping for crystal structural orientation. The red color indicates the sample surface is close to (001) plane as shown in the bottom color map. (d) The reproduced pole figures for lattice plane {0001} and {10-10}. Panels (e) and (f) are the *in situ* SEM EDX mapping for N- $K_{\alpha}$  and Nb- $L_{\alpha}$  lines respectively of the crystal. (g) The overlapping of Kikuchi pattern and EBSD pattern of the hexagonal  $\epsilon$ -NbN phase.

In order to exclude the proximity effect on multiphase powder specimens which includes a superconducting ingredient, we have developed an innovative technique to directly measure the electrical resistivity of  $\mu\text{m}$ -size cubic  $\delta$ - and hexagonal  $\epsilon$ -NbN single crystals. We first identified the micro-size single crystals of  $\delta$ - and  $\epsilon$ -NbN by electron backscattering diffraction technique (EBSD) using JEOL JSM-7800F Prime. The cubic  $\delta$ - and hexagonal  $\epsilon$ -NbN single crystals are then loaded to specially designed platforms fabricated by lithography and focused ion beam method respectively, which are specifically suitable to the four-probe electrical measurement in the Physical Property Measurement System (PPMS) from Quantum Design, Inc.

A tiny particle with size of  $50 \times 30 \times 5 \mu\text{m}^3$  was selected from commercial powder of  $\delta$ -NbN (Alfa Aesar Co.). The specimen was polished to satisfy the strict measurement criterion of EBSD for identifying the exact NbN phase. It was

first buried in epoxy for metallurgy polishing; a flat surface of the particle is shown by a SEM (scanning electron microscope) image in Fig. 5(a). The cubic  $\delta$ -NbN of the particle is confirmed by EBSD [Fig. 5(b)], which was identified as a single crystal of the scanning plane with (101) surface shown in the inverse pole figure mapping [Fig. 5(c)]. The reproduced pole figures for the lattice plane are {100}, {110}, and {111} as shown in Fig. 5(d). In the *in situ* SEM EDX mapping, red color represents N- $K_{\alpha}$  lines [Fig. 5(e)] and pink color represents Nb- $L_{\alpha}$  lines [Fig. 5(f)] of the crystal. The cubic  $\delta$ -NbN was identified by well overlapping the calculated Kikuchi and measured EBSD patterns [Fig. 5(g)] from which the lattice parameter  $a$  was estimated to be  $4.385(5) \text{ \AA}$ .

Figure 6(a) displays the image of the sample and platform. In Fig. 6(b), a drawing shows the center of the platform with 16 parallel Au electrodes  $2 \mu\text{m}$  in width deposited on a  $\text{SiO}_2/\text{Si}$  substrate. The polished  $\mu\text{m}$ -size  $\delta$  crystal was

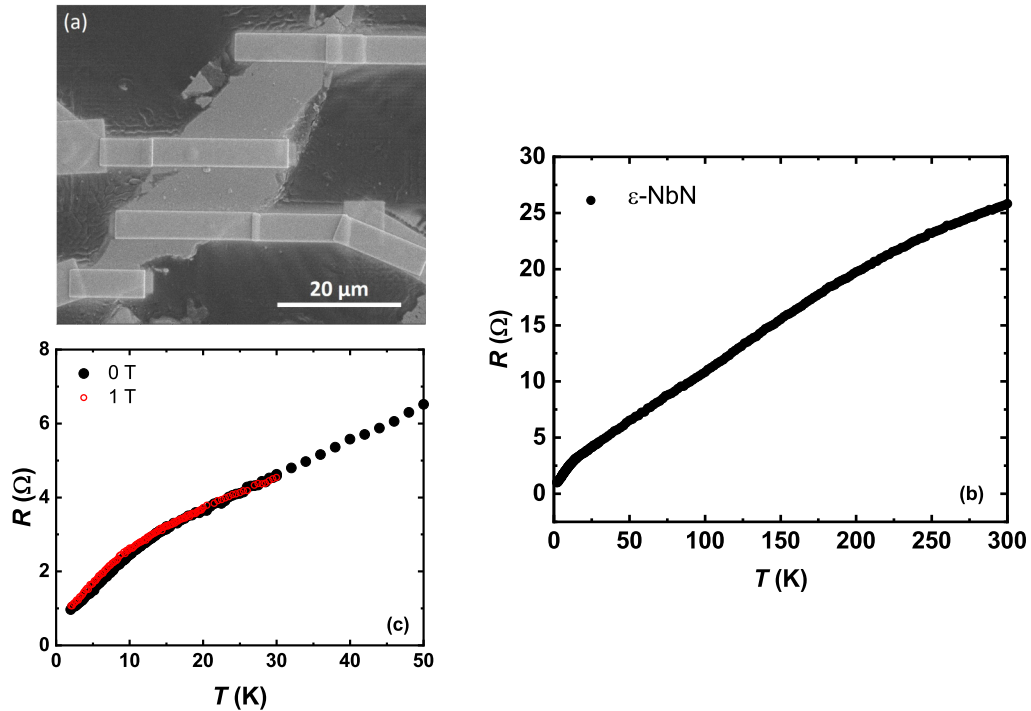


FIG. 9. (a) The SEM image of the  $\epsilon$ -NbN crystal with four electrodes for electrical resistance measurements. (b) Temperature dependence of electrical resistance of the  $\epsilon$ -NbN crystal; no superconductivity was discovered. (c) Temperature dependence of electrical resistance of the  $\epsilon$ -NbN crystal in 0 and 1 T at low temperatures.

transformed to the platform with the flat side in contact with electrodes for measuring resistivity [Fig. 6(a)]. The temperature dependence of electrical resistivity of the  $\delta$ -NbN crystal is shown in Fig. 6(c). The data reveal the resistive superconducting transition with onset  $T_c$  of 12.8 K, which is in good agreement with that of the cubic NbN single crystals reported [28,29]. It is known that the  $T_c$  of  $\delta$ -NbN is sensitively influenced by the stoichiometry of the specimen [25]. From the  $T_c$  value, we estimated this specific  $\mu\text{m}$ -size crystal having a  $\sim 25\%$  nitrogen deficiency which is supported by the result of the field emission electron probe microanalyzer (EPMA). The temperature dependence of resistivity under a magnetic field is shown in Fig. 7(a). The superconducting transition temperature is suppressed to 6.6 K as magnetic field up to 9 T. The estimated upper critical field at zero temperature,  $H_{C2}(0)$ , is about 21.3 T, using the formula of  $H_{C2}(T) = H_{C2}(0)[1 - (T/T_c)^{3/2}]^{3/2}$  [32,33] [Fig. 7(b)].

Using a similar method of sample characterization and preparation, a hexagonal  $\epsilon$ -NbN crystal with size of  $50 \times 20 \times 5 \mu\text{m}^3$  was obtained from a mix-phase powder from Goodfellow Corp. The SEM image of the crystal is shown in Fig. 8(a). The  $\epsilon$ -NbN phase was confirmed by EBSD phase map in Fig. 8(b). The sample surface close to the (001) plane is identified by the inverse pole figure mapping of the crystal in Fig. 8(c). The reproduced pole figures of the crystal for the lattice plane  $\{0001\}$  and  $\{10\cdot10\}$  are shown in Fig. 8(d). The *in situ* SEM EDX mapping for N- $K_\alpha$  and Nb- $L_\alpha$  lines of the crystal are shown in Figs. 8(e) and 8(f) respectively. The hexagonal  $\epsilon$ -NbN was demonstrated by good overlapping of calculated Kikuchi and measured EBSD patterns [Fig. 8(g)].

To examine whether the  $\epsilon$  crystal is superconducting or not, the  $\epsilon$  crystal was contacted by four Pt electrodes for resistance measurement using a focused ion beam (DBFIB-SEM, FEI Nova 600 NanoLab) [Fig. 9(a)]. The temperature dependence of electrical resistance of the  $\epsilon$  crystal at 2–300 K is shown in Fig. 9(b). The resistance exhibiting a metalliclike behavior without any superconducting transition was observed at all temperatures. No change in the resistance measurement at magnetic field of 1 T was observed below 30 K; this consequence further confirms the  $\epsilon$  crystal is not a superconductor [Fig. 9(c)]. The result is in good agreement with the earlier experimental work on  $\epsilon$ -NbN by Oya and Onodera [7], in which no superconductivity is observed for  $T > 1.77$  K and also consistent with the theoretical prediction by Li and Liu [19], Anand *et al.* [30], and Babu and Guo [21]. Furthermore, the high quality of the single crystal was also demonstrated by high residual resistance ratio (RRR) of 26.6 which is much larger than 1 of NbN films [34–37].

#### IV. CONCLUSION

We have characterized the structure and the electrical resistivity of  $\mu\text{m}$ -size single crystals of NbN. Combining the x-ray diffraction, magnetization, and specific heat measurements, we characterized the structural, transport, and magnetic properties of two powder specimens; one is a pure cubic  $\delta$ -NbN powder and the other is a multiphase powder with hexagonal  $\epsilon$ -NbN as the major phase. The magnetic, specific heat, and electrical conductivity data confirmed the superconductivity in cubic  $\delta$ -NbN. For the multiphase powder with hexagonal  $\epsilon$ -NbN as the major phase, two superconducting

transitions observed at 17.1 and 11.6 K observed in magnetic measurements can be clearly attributed to the impurity phases of cubic  $\delta$ - and tetragonal  $\gamma$ -NbN respectively in the specimen. In order to exclude the proximity effect on multi-phase powder specimens which includes the superconducting ingredient, we made innovative platforms to directly measure the electrical resistance of the single  $\mu\text{m}$ -size crystals, which are obtained from the  $\delta$ - and  $\varepsilon$ -NbN powders supplied by Alfa Aesar and Goodfellow, respectively. These small crystals are phase identified by electron backscattering diffraction technique (EBSD). The direct resistivity measurements on the  $\mu\text{m}$ -size crystals provide a concrete evidence that only cubic  $\delta$ -NbN is a superconductor whereas hexagonal  $\varepsilon$ -NbN is nonsuperconducting. The technique that can directly measure

a  $\mu\text{m}$ -size crystal provides a tool in helping resolve important scientific debates.

#### ACKNOWLEDGMENTS

We would like to thank Prof. C. S. Lin and Y. T. Lee in the Instrumentation Center, National Taiwan University for FEG-SEM measurements, and the technical support of Dr. W.-C. Lai from the Quantum Materials Shared Facilities of Institute of Physics at Academia Sinica. The work was supported by Ministry of Science and Technology Grants No. MOST 109-2112-M-001-010, No. 109-2112-M-001-047, and No. 110-2112-M-001-064.

- 
- [1] Y. Zuo, X. Wang, T. Chen, X. Li, X. Qi, D. Welch, P. Zhu, B. Liu, T. Cui, and B. Li, *Sci. Rep.* **5**, 10811 (2015).
- [2] R. Setzu, E. Baggetta, and J. C. Villégier, *J. Phys.: Conf. Ser.* **97**, 012077 (2008).
- [3] C. Benvenuti, P. Chiggiato, L. Parrini, and R. Russo, *Nucl. Instrum. Methods Phys. Res. A* **336**, 16 (1993).
- [4] M. Lindgren, M. Currie, W.-S. Zeng, R. Sobolewski, S. Cherednichenko, B. Voronov, and G. N. Gol'tsman, *Appl. Supercond.* **6**, 423 (1998).
- [5] N. Terao, *Jpn. J. Appl. Phys.* **4**, 353 (1965).
- [6] H. A. Johansen, R. E. Gold, and N. Pessall, *J. Phys. Chem. Solids* **29**, 19 (1968).
- [7] G. i. Oya and Y. Onodera, *J. Appl. Phys.* **45**, 1389 (1974).
- [8] E. C. Ethridge, S. C. Erwin, and W. E. Pickett, *Phys. Rev. B* **52**, R8589 (1995).
- [9] E. C. Ethridge, S. C. Erwin, and W. E. Pickett, *Phys. Rev. B* **53**, 12563 (1996).
- [10] N. Schoenberg, *Acta Metall.* **2**, 427 (1954).
- [11] G. I. Oya and Y. Onodera, *J. Appl. Phys.* **47**, 2833 (1976).
- [12] R. Sanjinés, M. Benkahoul, C. S. Sandu, P. E. Schmid, and F. Lévy, *Thin Solid Films* **494**, 190 (2006).
- [13] R. Kaiser, W. Spengler, S. Schickanz, and C. Politis, *Phys. Status Solidi B* **87**, 565 (1978).
- [14] W. Martienssen and H. Warlimont, in *Springer Handbook of Condensed Matter and Materials Data* (Springer, New York, 2005), p. 704.
- [15] V. Buscaglia, F. Caracciolo, M. Ferretti, M. Minguzzi, and R. Musenich, *J. Alloys Compd.* **266**, 201 (1998).
- [16] Y. Zou, X. Qi, C. Zhang, S. Ma, W. Zhang, Y. Li, T. Chen, X. Wang, Z. Chen, D. Welch, P. Zhu, B. Liu, Q. Li, T. Cui, and B. Li, *Sci. Rep.* **6**, 22330 (2016).
- [17] C. Wang, M. Wen, Y. D. Su, L. Xu, C. Q. Qu, Y. J. Zhang, L. Qiao, S. S. Yu, W. T. Zheng, and Q. Jiang, *Solid State Commun.* **149**, 725 (2009).
- [18] V. I. Ivashchenko, P. E. A. Turchi, and E. I. Olifan, *Phys. Rev. B* **82**, 054109 (2010).
- [19] X. F. Li and Z. L. Liu, *J. At. Mol. Sci.* **3**, 78 (2012).
- [20] P. J. Chen, W. J. Li, and T. K. Lee, *Phys. Rev. B* **104**, 115161 (2021).
- [21] K. R. Babu and G.-Y. Guo, *Phys. Rev. B* **99**, 104508 (2019).
- [22] Randolph E. Treece, James S. Horwitz, Douglas B. Chrisey, Edward P. Donovan, and Syed B. Qadri, *Chem. Mater.* **6**, 2205 (1994).
- [23] S. Linzen, M. Ziegler, O. V. Astafiev, M. Schmelz, U. Hübner, M. Diegel, E. Il'ichev, and H.-G. Meyer, *Supercond. Sci. Technol.* **30**, 035010 (2017).
- [24] M. Joguët, W. Lengauer, M. Bohn, and J. Bauer, *J. Alloys Compd.* **269**, 233 (1998).
- [25] A. V. Linde, R. M. Matin-Ayral, F. Bosc-Rouessac, and V. V. Grachev., *Int. J. Self-Propag. High-Temp. Synth.* **19**, 9 (2010).
- [26] Y. M. Shy, L. E. Toth, and R. Somasundaram, *J. Appl. Phys.* **44**, 5539 (1973).
- [27] R. E. Treece, M. S. Osofsky, E. F. Skelton, S. B. Qadri, J. S. Horwitz, and D. B. Chrisey, *Phys. Rev. B* **51**, 9356 (1995).
- [28] X.-J. Chen, V. V. Struzhkin, S. Kung, H.-k. Mao, R. J. Hemley, and A. N. Christensen, *Phys. Rev. B* **70**, 014501 (2004).
- [29] X.-J. Chen, V. V. Struzhkin, Z. Wu, R. E. Cohen, S. Kung, H.-k. Mao, R. J. Hemley, and A. N. Christensen, *Phys. Rev. B* **72**, 094514 (2005).
- [30] S. Anand, K. Thekkepat, and U. V. Waghmare, *Nano Lett.* **16**, 126 (2016).
- [31] Y. Y. Chen, P. C. Chen, C. B. Tsai, K. I. Suga, and K. Kindo, *Int. J. Thermophys.* **30**, 316 (2009).
- [32] A. B. Karki, Y. M. Xiong, N. Haldolaarachchige, S. Stadler, I. Vekhter, P. W. Adams, and J. Y. Chan, *Phys. Rev. B* **83**, 144525 (2011).
- [33] M. P. Mathur, D. W. Deis, and J. R. Gavaler, *J. Appl. Phys.* **43**, 3158 (1972).
- [34] S. Thakoor, J. L. Lamb, A. P. Thakoor, and S. K. Khanna, *J. Appl. Phys.* **58**, 4643 (1985).
- [35] U. Burkhardt, H. Bormann, P. Moll, M. Schmidt, Y. Grin, and A. Winklmann, *Sci. Rep.* **10**, 4065 (2020).
- [36] U. Burkhardt, A. Winkelmann, H. Bormann, A. Dumitriu, M. König, G. Cios, and Y. Grin, *Sci. Adv.* **7**, eabg0868 (2021).
- [37] A. Altinkök, *J. Naval Sci. Eng.* **16**, 71 (2020).